RSC Applied Interfaces

Accepted Manuscript

This article can be cited before page numbers have been issued, to do this please use: Y. Suzuki, K. Ito and K. Noda, *RSC Appl. Interfaces*, 2026, DOI: 10.1039/D6LF00160B.

ROYAL SOCIETY OF CHEMISTRY

rsc.li/RSCApplInter

View Article Online
DOI: 10.1039/D6LF00160B

ARTICLE

Band alignment estimation of MoS_2/g-C_3N_4 thin-film S-scheme heterojunction based on surface potential measurements

Received 00th January 20xx,
Accepted 00th January 20xx

DOI: 10.1039/x0xx00000x

Yuto Suzuki,[a] Kosei Ito,[b] and Kei Noda *[a]

Energy band alignment of thin-film heterojunction of molybdenum disulfide (MoS_2) and polymeric carbon nitride (g-C_3N_4) has been investigated, which can be regarded as a model system of heterojunction photocatalysts. A bilayer of MoS_2 and g-C_3N_4 (MoS_2/g-C_3N_4) with an exposed platinum (Pt) bottom electrode was fabricated by thermal chemical vapor deposition and sulfur hexafluoride-based dry etching, followed by deposition of MoS_2 nanosheets on top of that via tape exfoliation and elastomer-assisted transfer techniques. Simultaneous imaging of topography and surface potential over MoS_2/g-C_3N_4 on Pt was performed by using Kelvin probe force microscopy (KPFM) in dark. The energy band alignment of MoS_2/g-C_3N_4 on Pt was estimated based on the KPFM imaging results and other physical properties of individual MoS_2 and g-C_3N_4 samples examined with ultraviolet photoelectron spectroscopy and ultraviolet–visible absorption spectroscopy. In addition, photo-induced change in the surface potential over MoS_2/g-C_3N_4 on Pt was measured to consider the behavior of photo-induced carriers therein. The depicted energy band alignment having band bending in MoS_2 layer suggests the possibility of S-scheme heterojunction formation at the MoS_2/g-C_3N_4 interface.

Introduction

Photocatalytic technologies utilizing solar energy have attracted significant attention in the environmental and energy research and industry fields toward the realization of a sustainable society.[1–3] To enhance photocatalytic performance, it is essential to extend the light absorption range of photocatalysts to effectively utilize the solar spectrum, as well as to promote the separation of photo-induced charge carriers, namely electrons and holes. Heterojunction photocatalysts composed of different semiconductor materials have been extensively investigated for satisfying both requirements, where staggered band alignment is expected to spatially separate photo-induced electrons and holes, thereby suppressing their recombination.[4,5]

To date, n-type compound semiconductors have been most widely employed as photocatalysts. It has been reported that the formation of heterojunctions between two n-type semiconductors significantly enhances photocatalytic activity compared to their individual counterparts.[6–8] In recent years, photocatalytic research has increasingly focused on layered two-dimensional materials, such as transition metal dichalcogenides (TMDCs) and MXenes, owing to their excellent charge carrier transport and tunable physical properties. The number of studies applying these materials to heterojunction photocatalysts has also been growing.[9–11]

A thorough understanding of the local band alignment and charge carrier behavior at heterojunction interfaces is critically important to establish materials design guidelines for heterojunction photocatalysts. However, conventional approaches for investigating such properties have predominantly relied on macroscopic characterization techniques applied to powder samples, including ultraviolet-visible (UV–vis) absorption, X-ray photoelectron (XPS), and time-resolved photoluminescence (TRPL) spectroscopy.[12,13] These methods inherently suffer from limitations in elucidating charge carrier behaviors locally at heterojunction interfaces. Kelvin probe force microscopy (KPFM) is essentially the only technique capable of addressing this issue. KPFM enables the simultaneous imaging of surface topography and local work function or contact potential difference, making it a powerful tool for evaluating band alignment at heterojunction interfaces and quantitatively probing charge carrier separation under light irradiation.[14–19] Nevertheless, KPFM measurements require relatively flat, film-like samples, rendering the observation of conventional powder photocatalysts challenging. Although recent studies have applied KPFM to measure surface photovoltages in powder samples, many of these measurements were conducted on highly rough surfaces, making it difficult to estimate local band alignment from the obtained results.

Photocatalytic materials composed of layered two-dimensional substances can offer thin-film samples promising for KPFM measurements. Therefore, we focused on polymeric carbon nitride (g-C_3N_4) and molybdenum disulfide (MoS_2) as representative layered two-dimensional materials. g-C_3N_4 is a polymeric n-type semiconductor composed solely of carbon and nitrogen and has been extensively studied as a visible-light-

[a] Department of Electronics and Electrical Engineering, Keio University, 3-14-1, Hiyoshi, Kohoku-ku, Yokohama, 223-8522, Japan. E-mail: nodakei@elec.keio.ac.jp
[b] Department of Chemistry, Tokyo Metropolitan University, 1-1 Minami Osawa, Hachioji, Tokyo 192-0397, Japan.

View Article Online
DOI: 10.1039/D6LF00160B

responsive photocatalyst with a bandgap of approximately 2.7 eV, as well as excellent thermal and chemical stability.[20] Moreover, g-C_3N_4 can be deposited in the form of nanoparticles or thin films via thermal chemical vapor deposition (thermal CVD), enabling the fabrication of film-like samples suitable for KPFM observation. MoS_2, one of the most representative TMDCs, possesses a narrow bandgap of approximately 1.8 eV in the monolayer form and 1.3–1.5 eV in multilayer and bulk forms, along with high electron mobility. Therefore it has been widely investigated as an efficient electron donor for reduction reactions under visible-light irradiation.[21–23] In addition, numerous fabrication methods for MoS_2 nanosheets have been reported, and MoS_2/g-C_3N_4 heterojunction powder photocatalysts have demonstrated remarkably enhanced photocatalytic performance compared with the individual components, including hydrogen evolution under visible light,[24] degradation of volatile organic compounds[25] and dye.[26] These previous works suggest that MoS_2/g-C_3N_4 heterojunctions possess an efficient charge separation mechanism and are therefore highly suitable as model systems for KPFM observation.

In this study, a g-C_3N_4 thin film was deposited by thermal CVD onto a platinum (Pt) thin film electrode prepared on a Si wafer beforehand, and the g-C_3N_4 film surface was partially masked with another Si wafer and subjected to sulfur hexafluoride(SF_6)-based dry etching to expose the underlying Pt thin film as a reference electrode. MoS_2 nanosheets were then deposited by tape exfoliation and elastomer-assisted transfer methods in the vicinity of the boundary between the g-C_3N_4 and the Pt thin film. Thus, the fabricated sample structure with the exposed Pt reference electrode (as schematically drawn in Fig. 1) enabled more reliable surface potential imaging over MoS_2/g-C_3N_4. Surface potential measurements on MoS_2 nanosheets with various thicknesses were also performed to investigate the band bending in the MoS_2 layer deposited on the g-C_3N_4 film. Besides, the valence band maximum (VBM) positions, the optical bandgaps, and the majority carrier types of the respective MoS_2 and g-C_3N_4 layers were evaluated by ultraviolet photoelectron spectroscopy (UPS), UV–vis absorption spectroscopy, and electrochemical Mott–Schottky analysis, respectively. By combining this energy band information with the surface potential values obtained by KPFM, the possible band alignment for the MoS_2/g-C_3N_4 heterojunction on Pt electrode was discussed, which was supported by KPFM measurements under UV light irradiation.

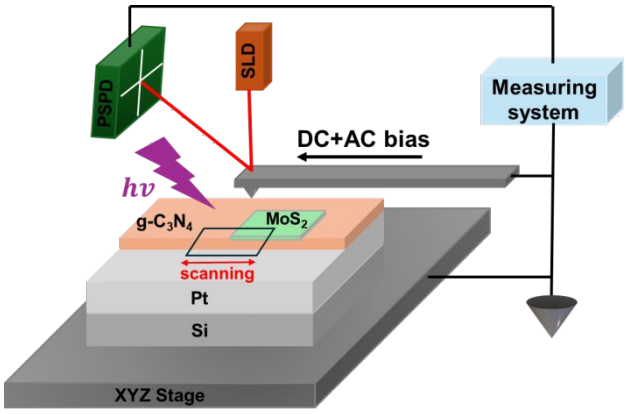

Fig. 1. Schematic illustration of the MoS_2/g-C_3N_4 bilayer sample with the exposed Pt electrode (MoS_2/g-C_3N_4/Pt) and Kelvin probe force microscopy (KPFM) measurements applied to the present sample.

Experimental

Preparation of MoS_2/g-C_3N_4 bilayers with exposed Pt electrodes

MoS_2/g-C_3N_4 bilayer samples for surface potential imaging were fabricated as follows. A 30-nm-thick Pt thin film was deposited onto a Si wafer (1.5 cm × 1.5 cm) with a DC sputtering system (SVC-700TMSG, Sanyu Electron). A g-C_3N_4 thin film was grown on the Pt-coated Si substrate by using our home-made thermal CVD apparatus using melamine powder (0.25 g) as the precursor.[27] After the substrate and the precursor were placed in a quartz tube furnace, the quartz tube was evacuated to a pressure of 40–133 Pa, followed by the introduction of an argon flow (1.5 sccm). Next, the melamine precursor was heated to 350 °C, while the temperature at the front and rear part of the quartz tube was maintained to be 750 °C and 400 °C for 30 min, respectively. After natural cooling, a uniform pale-yellow g-C_3N_4 film with a thickness of 20 nm was obtained. Then, half of the g-C_3N_4 film surface was masked and etched with SF_6 gas (50 sccm, 2 min) in a vacuum (10^{-3} Pa) by using a reactive ion etching system (CSE-1110, ULVAC) at a radio frequency power of 100 W, to expose the underlying Pt layer used as the bottom electrode for KPFM imaging as illustrated in Fig. 1.

MoS_2 nanosheets were prepared from bulk 2H-MoS_2 by Scotch tape exfoliation followed by elastomer-assisted transfer.[28,29] A polydimethylsiloxane (PDMS) stamp was fabricated by mixing a base polymer (KE-1606, Shin-Etsu Chemical) and curing agent (CAT-RG, Shin-Etsu Chemical) at a 6:1 ratio and curing at 80 °C for 1 h. The MoS_2 nanosheets were transferred onto the g-C_3N_4 film after the dry etching process, forming the MoS_2/g-C_3N_4 bilayer sample with exposed Pt electrodes (named as MoS_2/g-C_3N_4/Pt). Finally, the MoS_2/g-C_3N_4/Pt sample was finally vacuum-annealed at 200 °C for 1 h (AVO-200NB, AS ONE) to improve interfacial contact and remove surface adsorbates.[30]

Pristine MoS_2 nanosheets and g-C_3N_4 films on Pt layers (named as MoS_2/Pt and g-C_3N_4/Pt, respectively) were also prepared under identical conditions to those used for the MoS_2/g-C_3N_4/Pt sample preparation, and were utilized to determine the energy band structures of each material.

Structural and physical characterization

Surface morphologies of thin film samples were observed by atomic force microscopy (AFM; Innova SPM, Bruker AXS) using a Pt-coated Si cantilever (Olympus OMCL-AC240TM). The nominal resonance frequency and spring constant of the cantilever were 70 kHz and 2 N/m, respectively. Measurements were performed under ambient conditions at a scan rate of 0.4

Hz per line. Elemental composition and chemical bonding states of the MoS_2 and g-C_3N_4 thin films were analyzed with an XPS instrument (Nexsa G2, Thermo Fisher Scientific) using Mg Kα radiation (hv = 1253.6 eV), with the binding energy calibrated to the C 1s peak at 284.8 eV. Crystal structures of the MoS_2 and g-C_3N_4 thin films were examined by X-ray diffraction (XRD; D8 Advance, Bruker). UV–Vis diffuse reflectance spectra were collected using a UV–Vis–NIR spectrophotometer equipped with an integrating sphere (UV-3600Plus, Shimadzu) and converted using the Kubelka–Munk function. Optical bandgaps were estimated from Tauc plots assuming indirect transitions.

VBM position (E_{VBM}) was determined by ultraviolet photoelectron spectroscopy (UPS; Nexsa G2, Thermo Fisher Scientific) using He I radiation (hv = 21.2 eV). E_{VBM} was calculated from the high-binding-energy cutoff (E_{cutoff}), the onset energy in the valence band edge region (E_{onset}), and the following formula: $E_{VBM} = 21.2 - (E_{cutoff} - E_{onset})$.

Conduction types of carriers in the materials were identified by electrochemical Mott–Schottky analysis in aqueous Na_2SO_4 electrolyte, using a three-electrode configuration with MoS_2 or g-C_3N_4 as the working electrode, a Pt wire as the counter electrode, and an Ag/AgCl (RE-1B, BAS Inc.) as the reference electrode. A potentiostat (VersaSTAT3, AMETEK Scientific Instruments) was utilized on condition that the modulation frequency and amplitude were set to 1 kHz and 10 mV, respectively.

Surface potential imaging

Surface potential mapping was performed by using an AFM system (Innova SPM, Bruker AXS) in the frequency-modulation KPFM (FM-KPFM) mode,[31] while surface topography was simultaneously observed in the tapping mode. In FM-KPFM, a modulation bias voltage (1.5 kHz, 2 V peak-to-peak) was applied between the Pt-coated Si cantilever (OMCL-AC240TM, Olympus) and the Pt bottom electrode of the samples prepared in this study. The nominal resonance frequency and spring constant of the cantilever were 70 kHz and 2 N/m, respectively. The scan rate was set to 0.4 Hz, and images were acquired with a resolution of 128 × 128 pixels. The resulting electrostatic force-gradient signal was extracted from the phase signal of the cantilever vibration using a lock-in amplifier (LI5640, NF Circuits) and fed into a custom-built proportional–integral (PI) controller. The DC bias voltage was adjusted to minimize the electrostatic force gradient, so that the contact potential difference between the AFM tip and the sample surface was determined. The whole AFM system was enclosed in a light-shielded box to eliminate ambient light.

KPFM images obtained under dark and UV illumination for the MoS_2/g-C_3N_4/Pt sample were compared to examine photo-induced surface potential changes. UV light (300–400 nm, 1.2 W/m^2) from a xenon lamp (LAX-101, Asahi Spectra) was employed. In this study, all the AFM/KPFM observations were conducted under ambient conditions.

Results and discussion

Morphological characterization of MoS_2/g-C_3N_4/Pt sample

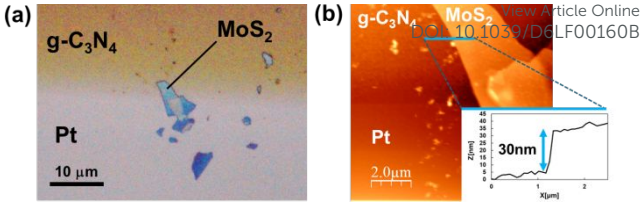

Fig. 2. (a) Optical microscope and (b) AFM topography image of the MoS_2/g-C_3N_4/Pt sample. The height profile of a MoS_2 nanosheet on the g-C_3N_4 film is presented in the inset. The thickness of the MoS_2 nanosheet was measured to be 30 nm.

The morphology of the MoS_2/g-C_3N_4/Pt sample was examined by optical microscopy (OM) and AFM. The OM image (Fig. 2a) shows that MoS_2 flakes with lateral sizes of several micrometers are deposited near the interface between the g-C_3N_4 thin film and the Pt substrate. The clear optical contrast among MoS_2, g-C_3N_4, and Pt enables straightforward identification of the individual regions. The AFM topography image (Fig. 2b) confirms the formation of well-defined boundaries among 30-nm-thick MoS_2, g-C_3N_4, and Pt. The CVD-grown g-C_3N_4 surface in Fig. 2b exhibits a smooth morphology with a root-mean-square (RMS) roughness of 1.55 nm (Fig. S1a (SI)), which is comparable to that of the pristine g-C_3N_4 film on Pt on Si substrate (Pt/Si) (1.60 nm; Fig. S1b (SI)), indicating that the sample preparation of MoS_2/g-C_3N_4/Pt does not alter the g-C_3N_4 surface morphology. Similarly, the MoS_2 region on the g-C_3N_4 film (Fig. S1c (SI)) and pristine MoS_2 nanosheets on Pt (Fig. S1d (SI)) show comparable RMS roughness values of 0.46 nm, demonstrating that the MoS_2 morphology is also unaffected by the MoS_2/g-C_3N_4 formation. Overall, the MoS_2/g-C_3N_4/Pt sample provides small surface roughness toward KPFM analysis.

Structural and physical characterization of g-C_3N_4 and MoS_2 samples

XPS analysis of g-C_3N_4/Pt revealed characteristic peaks in both C 1s (Fig. 3a) and N 1s (Fig. 3b) regions. The C 1s spectrum showed a peak at 284.8 eV corresponding to graphitic carbon (C–C bonding), along

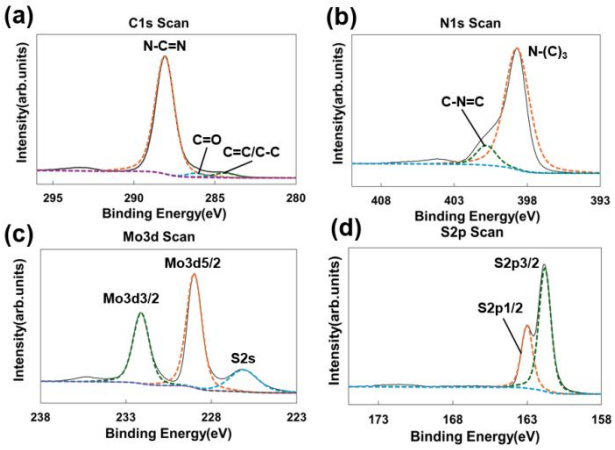

Fig. 3. XPS spectra of (a) C 1s and (b) N 1s for g-C_3N_4 thin film, and (c) Mo 3d and (d) S 2p for MoS_2 nanosheets.

View Article Online DOI: 10.1039/D6LF00160B

with additional peaks at 286.1 and 288.1 eV attributed to sp^2-hybridized carbon in N=C–N bonding environments. In the N 1s spectrum, a peak at 398.7 eV was assigned to C–N=C bonds, and a peak at 400.3 eV was attributed to tertiary nitrogen species (N–$(C)_3$).[32] Quantitative analysis indicated a carbon-to-nitrogen atomic ratio of 3:4.04 (C/N ≈ 0.74), which closely matches the theoretical stoichiometry of C_3N_4 (C/N = 0.75), suggesting that the g-C_3N_4 film was formed with near-stoichiometric composition.

The XPS spectra for MoS_2/Pt exhibited peaks in Mo 3d (Fig. 3c) and S 2p (Fig. 3d) regions. The Mo 3d spectrum displayed doublets at 228.1 eV (Mo 3d5/2) and 231.7 eV (Mo 3d3/2), corresponding to Mo^{4+} in MoS_2. The S 2p spectrum showed peaks at 161.2 eV (S 2p3/2) and 162.4 eV (S 2p1/2), that are characteristic of sulfur ions (S^{2-}).[33] These results confirm that the MoS_2 nanosheets retained the chemical state of pure 2H-phase MoS_2, composed of Mo^{4+} and S^{2-}.

XRD measurements revealed a characteristic (002) reflection associated with layered structures along the c-axis at 14.5° (with d spacing of 0.61 nm) for MoS_2 (Fig. S2a (SI)) and at 27.5° (with d spacing of 0.32 nm) for g-C_3N_4 (Fig. S2b (SI)). These results indicate the formation of layered structures along the c-axis and suggest that both materials possess two-dimensional structural characteristics.

UPS and UV–vis absorption measurements were carried out to elucidate the energy band diagrams of g-C_3N_4 and MoS_2.[34] In the measured UPS spectra (Fig. 4a and 4c), the values of E_{cutoff} and E_{onset} were estimated to be 19.5 eV and 4.35 eV for g-C_3N_4, 19.6 eV and 4.6 eV for MoS_2, respectively. Accordingly, the VBM positions with respect to the vacuum level were determined to be 6.05 eV for g-C_3N_4 and 6.2 eV for MoS_2, respectively. In addition, Tauc plots constructed from the UV–vis absorption spectra (Fig. 4b and 4d) were used to estimate the optical bandgap (E_g) by extrapolating the linear regions near the absorption edges. The resulting E_g values were calculated to be 2.62 eV for g-C_3N_4 and 1.48 eV for MoS_2, respectively. By using the estimated VBM positions and E_g values, the conduction band minimum (CBM) positions were calculated to be 3.43 eV for g-C_3N_4 and 4.72 eV for MoS_2, respectively. Additionally, Mott–Schottky plots (C^{-2}–V) obtained by electrochemical measurements (Fig. S3 (SI)) exhibit positive slopes, indicating that both the MoS_2 and g-C_3N_4 film prepared in this study are n-type semiconductors. Eventually, the energy band diagrams of the g-C_3N_4 and MoS_2 film estimated from these measurement results are given in Fig. 4e, where the obtained VBM and CBM positions are in line with the previously reported values.[35–37]

Surface potential imaging and energy band alignment estimation for MoS_2/g-C_3N_4/Pt sample

Figure 5a and 5b present the topography and surface potential image observed for the MoS_2/g-C_3N_4/Pt sample in dark under ambient conditions. In Fig. 5b, the surface potential (SP) on g-C_3N_4 is higher than that on Pt, and the SP on MoS_2/g-C_3N_4/Pt becomes lower than that on Pt. The SP values on the Pt, g-C_3N_4/Pt, and MoS_2/g-C_3N_4/Pt regions (indicated by the light blue boxes in Fig. 5b) were evaluated by fitting the histogram of the SP values at all pixels (totally 120 pixels) in each region[38] with a single Gaussian function including a constant background, and the resulting peak positions were obtained as the SP values (Fig. 5c–5e). It should be noted that the horizontal axis values of the histograms in Figs. 5c-5e correspond to the raw data values. Eventually, the SP on g-C_3N_4/Pt is 219 mV higher than that on Pt, while the SP on MoS_2/g-C_3N_4/Pt is 3 mV lower than that on Pt.

Successively, we investigated SP changes on the MoS_2/g-C_3N_4 layer against the thickness of MoS_2 to examine band bending in the MoS_2 layer. It should be noted that when the thickness of MoS_2 nanosheets approaches the few-layer regime, the energy band diagram of MoS_2 intrinsically changes with decreasing layer number.[39] Under such circumstances, it becomes difficult to discuss band bending effects based on MoS_2 thickness dependence of surface potential. Hence, MoS_2 nanosheets with thicknesses in the range from 10 to 45 nm were chosen and examined in this study.

Surface topography and potential images, thickness line profiles, and surface potential histograms obtained for MoS_2 nanosheets with various thicknesses are shown in Fig. S4–S8 (SI). All imaging

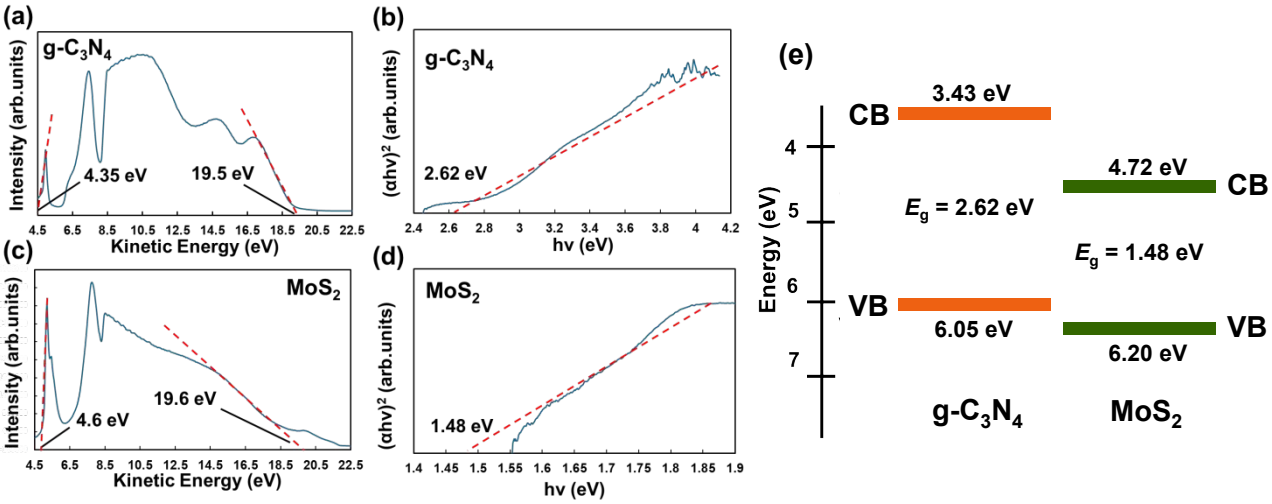

Fig. 4. (a, c) UPS spectra and (b, d) Tauc plot derived from UV–vis absorption spectra of the g-C_3N_4 and MoS_2 film, respectively. (e) Energy band diagrams of the g-C_3N_4 and MoS_2 film, estimated from the measured UPS and UV–vis spectra.

View Article Online
DOI: 10.1039/D6LF00160B

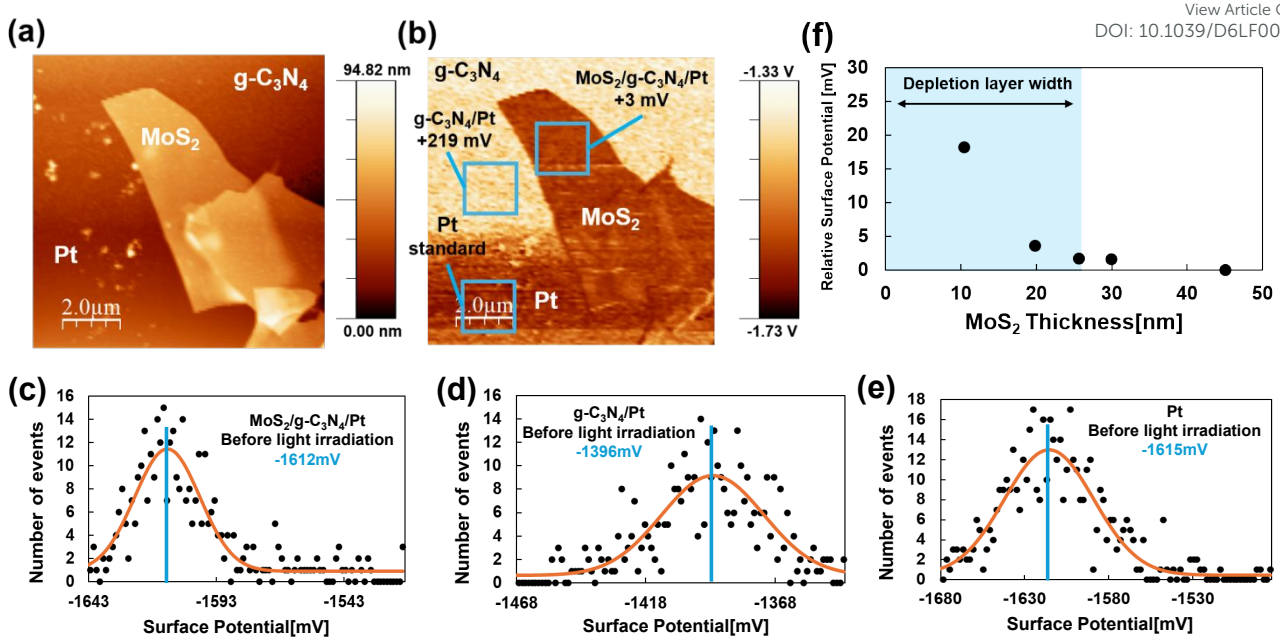

Fig. 5. (a) AFM topography and (b) surface potential (SP) image observed for the MoS_2/g-C_3N_4/Pt sample in dark. Surface potential histograms on (c) g-C_3N_4/Pt, (d) MoS_2/g-C_3N_4/Pt, and (e) Pt regions (indicated by the light blue boxes in Fig. b) are presented. (f) Relationship between MoS_2 thickness and the relative SP value on MoS_2/g-C_3N_4/Pt. The relative SP value is referenced to that of the sample with a 45-nm-thick MoS_2 layer.

experiments were performed in dark under ambient conditions, on the same day to ensure consistency of the experimental conditions. The SP values on MoS_2 nanosheets on g-C_3N_4/Pt were determined by fitting the SP histograms extracted from the regions of interest (blue boxes in the SP images) with Gaussian functions and extracting the peak positions. The relationship between the MoS_2 nanosheet thickness and the obtained peak SP values is provided in Fig. 5f, where the relative SP value is plotted relative to that of the sample with a 45-nm-thick MoS_2. As shown in Fig. 5f, the surface potential increases with decreasing MoS_2 thickness, which suggests the presence of downward band bending in the vicinity of the MoS_2/g-C_3N_4 interface. By considering the MoS_2 thickness value at which the surface potential begins to increase, the depletion width in the MoS_2 layer is roughly estimated to 25 nm.

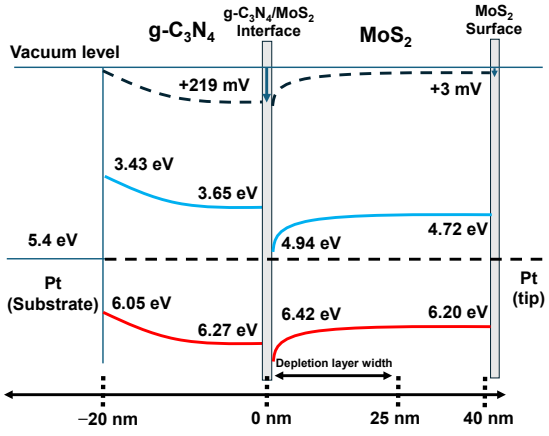

Fig. 6. Energy band alignment of the MoS_2/g-C_3N_4/Pt structure considered based on KPFM and other measurement results in this study. The values in the horizontal axis present the height with respect to the MoS_2/g-C_3N_4 interface position.

The energy band alignment for the MoS_2/g-C_3N_4/Pt sample was analyzed from the above-described results of SP measurements. First, as shown in Fig. 5b, the surface potential on g-C_3N_4/Pt is 219 mV higher than that on Pt, which indicates the presence of an internal electric field directed from g-C_3N_4 toward Pt. On the other hand, the surface potential on g-C_3N_4/Pt is 216 mV higher than that on MoS_2/g-C_3N_4/Pt, suggesting the formation of another internal electric field directed from g-C_3N_4 toward MoS_2 surface. Assuming that the work function of Pt is 5.4 eV,[40] Schottky barrier formation at the g-C_3N_4/Pt interface is a plausible scenario because of the estimated CBM position for n-type g-C_3N_4 thin film (3.43 eV). In addition, the downward band bending in MoS_2 layer (shown in Fig. 5f) and the obtained VBM and CBM positions for MoS_2 and g-C_3N_4 (presented in Fig. 4e) need to be considered at the same time.

The above-mentioned constraints result in an energy band alignment of the MoS_2/g-C_3N_4/Pt structure, as illustrated in Fig. 6. Here, the SP value of 219 mV on g-C_3N_4/Pt is interpreted as the magnitude of the band bending across the g-C_3N_4 layer. Additionally, the band bending magnitude across the MoS_2 layer on g-C_3N_4 is taken as 216 mV. These magnitudes and directions of band bending, along with the downward band bending near the MoS_2/g-C_3N_4 interface, are reflected in Fig. 6. This interfacial band bending at the MoS_2/g-C_3N_4 interface can support the so-called S-scheme heterojunction formation.[41-43] If we assume MoS_2/g-C_3N_4 as an S-scheme-based photocatalyst, MoS_2 would work as an oxidation photocatalyst (OP) and g-C_3N_4 would work as a reduction photocatalyst (RP), because the CBM position for g-C_3N_4 is higher than that of MoS_2 and both of them are n-type semiconductors.[40] According to the S-scheme mechanism, downward band bending in the OP side and upward

View Article Online
DOI: 10.1039/D6LF00166B

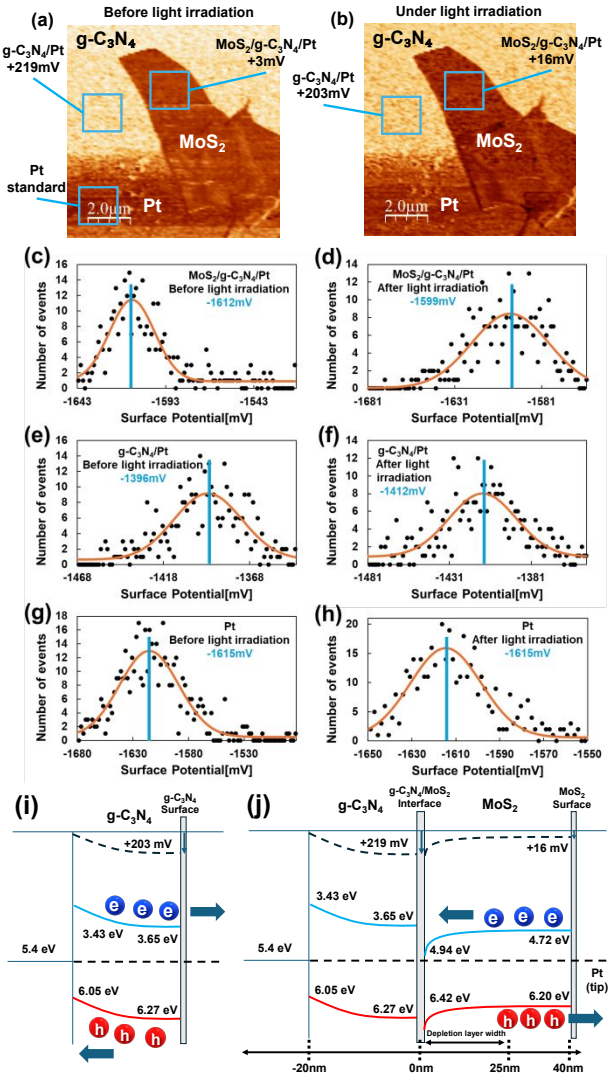

Fig. 7. Surface potential image observed for $MoS_2/g\text{-}C_3N_4/Pt$ sample (a) before and (b) under UV irradiation. Surface potential histograms extracted from KPFM images acquired (c, e, d) before and (d, f, h) under light irradiation for $MoS_2/g\text{-}C_3N_4/Pt$ (c, d), $g\text{-}C_3N_4/Pt$ (e, f), and Pt (g, h) regions. Schematic illustrations of the photo-induced charge separation behavior inferred from the band alignment are presented for (i) the $g\text{-}C_3N_4/Pt$ interface and (j) the $MoS_2/g\text{-}C_3N_4/Pt$ structure. Here, the generated electrons and holes are depicted, with solid arrows indicating the possible migration directions of these photo-induced carriers.

band bending in the RP side can occur at the heterojunction of OP and RP, which is in line with the downward band bending in the MoS_2 layer observed in this study. Indeed, experimental studies on heterojunction photocatalysts have actively discussed that physically-contacted $MoS_2/g\text{-}C_3N_4$ composite photocatalysts exhibit S-scheme-dominated charge transfer rather than conventional type-II behavior with negligible interfacial band bending.[44]

Surface potential imaging for $MoS_2/g\text{-}C_3N_4/Pt$ sample under light irradiation

KPFM measurement for $MoS_2/g\text{-}C_3N_4/Pt$ sample under light irradiation was performed to examine whether the photo-induced SP changes are consistent with the predicted band diagrams shown in Fig. 6. Surface potential images observed for $MoS_2/g\text{-}C_3N_4/Pt$ sample before and under UV irradiation are presented in Fig. 7a and 7b. The SP values on Pt, $g\text{-}C_3N_4/Pt$, and $MoS_2/g\text{-}C_3N_4/Pt$ regions before and under light irradiation were evaluated from histograms of the SP values at all pixels (120 pixels for each region) given in Fig. 7c–7h, by using the same procedure for obtaining results of Fig. 5c-5e. Please note that the horizontal axis values of the histograms in Fig. 7c-7h are the raw potential values. As a result, light irradiation gave rise to the SP increase by 13 mV on $MoS_2/g\text{-}C_3N_4/Pt$ and the SP decrease by 16 mV on $g\text{-}C_3N_4/Pt$, while no detectable surface potential shift was observed for the Pt reference.

The observed, photo-induced SP increase and decrease on $MoS_2/g\text{-}C_3N_4/Pt$ and $g\text{-}C_3N_4/Pt$ can be attributed to the hole accumulation on MoS_2 surface and the electron accumulation on $g\text{-}C_3N_4$ surface, respectively.[45] According to the energy band diagram for $MoS_2/g\text{-}C_3N_4/Pt$ structure (Fig. 6), photo-induced electrons produced in $g\text{-}C_3N_4$ are supposed to migrate toward $MoS_2/g\text{-}C_3N_4$ interface region, whereas photo-induced holes in $g\text{-}C_3N_4$ can be transported toward the Pt electrode, as illustrated in Fig. 7i. Likewise, photo-induced electrons produced in MoS_2 are likely to migrate toward $MoS_2/g\text{-}C_3N_4$ interface, while photo-induced holes in MoS_2 can flow into MoS_2 surface, as illustrated in Fig. 7j. These photo-induced charge separation and accumulation mechanisms discussed here are in good agreement with the KPFM observation results before and under light irradiation in this study. Consequently, it can be reasonably said that our results of surface potential imaging under light irradiation support the energy band alignments proposed in Fig. 6.

The introduction of the Pt reference electrode was indispensable for examining the band bending direction in each layer of MoS_2 and $g\text{-}C_3N_4$ from the surface potential data, and for determining the energy band alignment of the heterojunction under equilibrium conditions. On the other hand, the Pt electrode may influence the potential distribution within the $MoS_2/g\text{-}C_3N_4$ heterojunction system. To examine this influence, KPFM measurements on $MoS_2/g\text{-}C_3N_4/Pt$ samples with various thicknesses of $g\text{-}C_3N_4$ and MoS_2 will be pursued in future works. In particular, a thicker $g\text{-}C_3N_4$ film is expected to suppress the influence of the Pt electrode and the $g\text{-}C_3N_4/Pt$ interface on the $MoS_2/g\text{-}C_3N_4$ heterojunction, thereby enabling a more reliable estimation of the band alignment in the $MoS_2/g\text{-}C_3N_4$ system.

Conclusions

In this study, surface potential mapping using KPFM was performed for $MoS_2/g\text{-}C_3N_4/Pt$ sample fabricated by thermal CVD growth and SF_6-based etching of $g\text{-}C_3N_4$, followed by MoS_2 nanosheet deposition with tape exfoliation and elastomer-assisted transfer. The energy band alignment of $MoS_2/g\text{-}C_3N_4/Pt$ was estimated by combining the KPFM imaging results with physical properties of respective MoS_2 and $g\text{-}C_3N_4$ layers examined with various characterization methods. The KPFM measurements for the heterostructure samples with various

MoS_2 thicknesses suggest the downward band bending near the MoS_2/g-C_3N_4 interface, with the roughly estimated depletion width in the MoS_2 layer of ca. 25 nm. Finally, the depicted energy band alignment reveals the formation of a Schottky contact at the g-C_3N_4/Pt interface and the downward band bending within the MoS_2 layer, indicating an S-scheme heterojunction which could facilitate efficient charge separation. In addition, photo-induced changes in the surface potential over MoS_2/g-C_3N_4/Pt were explained by the hole accumulation on the MoS_2 surface and the electron accumulation on the g-C_3N_4 surface, which is in line with the estimated energy band alignment in this work.

Overall, this work demonstrates that scanning probe microscopy–based surface potential analysis is a powerful and effective approach for evaluating band alignment in photocatalytic heterojunctions. The present study contributes to bridging the gap between conventional bulk-averaged characterization methods and localized nanoscale analysis. Further systematic and comparative studies between KPFM observations and macroscopic photocatalytic measurements for various composite photocatalysts will be necessary to render our conclusions and methods applicable to a broader range of practical powder heterojunction photocatalysts.

Author contributions

Yuto Suzuki: investigation, methodology, data curation, writing – original draft; Kosei Ito: investigation, supervision, writing – review & editing; Kei Noda: conceptualization, methodology, supervision, funding acquisition, project administration, writing – review & editing.

Conflicts of interest

There are no conflicts to declare.

Data availability

All data supporting this study are available within the article and its supplementary information (SI). Supplementary information: AFM topography images of g-C_3N_4 and MoS_2 sample. XRD patterns of g-C_3N_4 and MoS_2 sample. Electrochemical Mott-Schottky plots of g-C_3N_4 and MoS_2 sample. AFM and KPFM observation results of MoS_2 nanosheets with various thicknesses. See DOI: https://doi.org/10.1039/0xx00000x.

Acknowledgements

The authors would like to thank Prof. Hirofumi Yamada for fruitful discussions and Prof. Kei Kobayashi for kind support in KPFM instrumentation. This study was supported by a Grant-in-Aid for Scientific Research (KAKENHI No. 25K01271) of the Japan Society for the Promotion of Science (JSPS).

Notes and references

(1) T. S. Teets and D. G. Nocera, *Chem. Commun.* 2011, **47,** 9268—9274.
(2) P. Shandilya, S. Sambyal, R. Sharma, P. Mandyal and B. Fang, *J. Hazard. Mater.* 2022, **428,** 128218.
(3) A. S. Kumar, D. P. Pabba, N. R. Reddy and S. W. Joo, *J. Alloys Compd.* 2025, **1031,** 180934.
(4) S. Nahar, M. F. M. Zain, A. H. Kadhum, H. A. Hasan and M. R. Hasan, *Materials* 2017, **10,** 629.
(5) R. Kumar, D. Das and A. K. Singh, *J. Catal.* 2018, **359,** 143—150.
(6) S. Asadi, J. B. Ghasemi, E. S. Ghalehsefid, M. Shekofteh-Gohari and M. Mousavi, *Mater. Chem. Phys.* 2025, **338,** 130575.
(7) A. V. Zhurenok, A. A. Sushnikova, A. A. Valeeva, A. Yu. Kurenkova, D. D. Mishchenko, E. A. Kozlova and A. A. Rempel, *Kinet. Catal.* 2024, **65,** 137—147.
(8) S. M. Albukhari, L. A. Al-Hajji and A. A. Ismail, *Renew. Energy* 2024, **228,** 120649.
(9) X.-R. Gan, D.-Y. Lei, R.-Q. Ye, H.-M. Zhao and K.-Y. Wong, *Nano Res.* 2021, **14,** 2003—2022.
(10) Y. Zhang, C.-H. Dong, Z. Ye, Y. Hou and S. Ye, *Chem. Commun.* 2025, **61,** 7158—7177.
(11) Z. K. Karakas and Z. Donmez, *Sustainability* 2025, **17,** 1904.
(12) P. Priyadarshini, A. Mishra, A. Majhi, K. Parida and K. M. Parida, *ACS Appl. Energy Mater.* 2025, **8,** 5067—5081.
(13) S. Das, L. Acharya, L. Biswal and K. Parida, *Nanoscale Adv.* 2024, **6,** 934—946.
(14) N. Satoh, M. Yamaki, K. Noda, S. Katori, K. Kobayashi, K. Matsushige and H. Yamada, *Jpn. J. Appl. Phys.* 2015, **54,** 08KF06.
(15) V. Palermo, M. Palma and P. Samorì, *Adv. Mater.* 2006, **18,** 145—164.
(16) R. Chen, F. Fan, T. Dittrich and C. Li, *Chem. Soc. Rev.* 2018, **47,** 8238—8262.
(17) H. Shim, A. S. Sharma, R. Mishra, J. Han, J. Lim, D. Zhang, Z. L. Teh, J. Park, J. Seidel, M. P. Nielsen, M. A. Green, S. Huang, J. S. Yun and J. Kim, *ACS Nano* 2024, **18,** 31002—31013.
(18) R. Kumar, D. Varandani and B. R. Mehta, *Carbon* 2016, **98,** 41—49.
(19) Z. Meng, J. Zhang, H. Long, H. García, L. Zhang, B. Zhu and J. Yu, *Angew. Chem. Int. Ed.* 2025, **64,** e202505456.
(20) J. Wen, J. Xie, X. Chen and X. Li, *Appl. Surf. Sci.* 2017, **391,** 72—123.
(21) T. F. Jaramillo, K. P. Jørgensen, J. Bonde, J. H. Nielsen, S. Horch and I. Chorkendorff, *Science* 2007, **317,** 100—102.
(22) S. Singh, A. Modak, K. K. Pant, A. Sinhamahapatra and P. Biswas, *ACS Appl. Nano Mater.* 2021, **4,** 8644—8667.
(23) Y.-C. Zhang, R.-J. Zhang, Y.-X. Guo, Y.-M. Li and K.-S. Li, *J. Alloys Compd.* 2024, **998,** 174916.
(24) Y. Fan, Y.-N. Yang and C. Ding, J. *Inorg. Organomet. Polym. Mater.* 2021, **31,** 4722—4730.
(25) Y.-M. Tian, L. Ge, K.-Y. Wang and Y.-S. Chai, *Mater. Charact.* 2014, **87,** 70—73.
(26) Z.-J. Lan, Y.-L. Yu, J.-H. Yao and Y.-A. Cao, *Mater. Res. Bull.* 2018, **102,** 433—439.
(27) K. Ito, S. Yoneyama, S. Yoneyama, P. Fons and K. Noda, *ACS Mater. Au* 2025, **5,** 299—307.
(28) H. Jang, I.-S. Kang, Y. Lee, Y. J. Cha, D. K. Yoon, C. W. Ahn and W. Lee, *Nanotechnology* 2016, **27,** 365705.
(29) L. Ottaviano, S. Palleschi, F. Perrozzi, G. D'Olimpio, F. Priante, M. Donarelli, P. Benassi, M. Nardone, M. Gonchigsuren, M. Gombosuren, A. Lucia, G. Moccia and O. A. Cacioppo, *2D Mater.* 2017, **4,** 045013.
(30) P. Budania, P. T. Baine, J. H. Montgomery, D. W. McNeill, S. J. N. Mitchell, M. Modreanu and P. K. Hurley, *Mater. Res. Express*, 2017, **4,** 025006.
(31) C. Li, S. Minne, Y. Hu, J. Ma, J. He, H. Mittel, V. Kelly, N. Erina, S. Guo and T. Mueller, Peak Force Kelvin Probe Force

View Article Online
DOI: 10.1039/D6LF00160B

Microscopy, Application Note #140, Bruker Nano Surfaces Division, Santa Barbara, CA 2013.
(32) S. Ganesan, T. Kokulnathan, S. Sumathi and A. Palaniappan, *Sci. Rep.* 2024, **14,** 2284.
(33) J. Kibsgaard, Z. Chen, B. N. Reinecke and T. F. Jaramillo, *Nat. Mater.* 2012, **11,** 963—969.
(34) C. Maheu, L. Cardenas, E. Puzenat, P. Afanasiev and C. Geantet, *Phys. Chem. Chem. Phys.* 2018, **20,** 25629—25637.
(35) I. Rapti, F. Bairamis and I. Konstantinou, *Photochem* 2021, **1**, 358—370.
(36) L. A. H. Jones, Z. Xing, J. E. N. Swallow, H. Shiel, T. J. Featherstone, M. J. Smiles, N. Fleck, P. K. Thakur, T.-L. Lee, L. J. Hardwick, D. O. Scanlon, A. Regoutz, T. D. Veal and V. R. Dhanak, *J. Phys. Chem. C* 2022, **126,** 21022—21033.
(37) S. Sarma, S. C. Ray and S. S. Singha, *J. Phys.: Condens. Mat.* 2019, **31,** 135501.
(38) I. Sharma and B. R. Mehta, *Appl. Phys. Lett.* 2017, **110,** 061602.
(39) D. Xie, F. Yang, X. Qiu, Y. Hu, Y. Sun, S. He and X. Wang, *Physica B* 2024, **684,** 415953.
(40) H.-J. Woo, W.-J. Lee, C.-M. Kim, Q. Wang, S. Zhang, Y.-J. Yoon and S.-H. Kwon, *Coatings* 2022, **12,** 101.
(41) L. Zhang, J. Zhang, H. Yu, J. Yu, *Adv. Mater.* 2022, **34,** 2107668.
(42) X. Wang, J. Ma, J. H. Fan, H. Zhu, X. M. Liu, H. Q. Xia and Y. T. Liu, *J. Chem. Inf. Model.* 2023, **63,** 4708.
(43) K. Ito, S. Fujioka, S. Yoneyama, M. R. Vosberg, P. Fons and K. Noda, *Appl. Surf. Sci.* 2026, **732,** 166558.
(44) A. H. Bashal, K. Alkanad, M. Al-Ghorbani, S. Ben Aoun and M. A. Bajiri, *J. Environ. Chem. Eng.* 2023, **11,** 109545.
(45) M. Ahmad, K. Agarwal, N. Kumari and B. R. Mehta, *Appl. Phys. Lett.* 2017, **111,** 023904.

View Article Online
DOI: 10.1039/D6LF00160B

Data availability

All data supporting this study are available within the article and its supplementary information (SI). Supplementary information: AFM topography images of g-C_3N_4 and MoS_2 sample. XRD patterns of g-C_3N_4 and MoS_2 sample. Electrochemical Mott-Schottky plots of g-C_3N_4 and MoS_2 sample. AFM and KPFM observation results of MoS_2 nanosheets with various thicknesses.